nanomaterials

MDPI

Communication

Quasi-2D $Mn_3Si_2Te_6$ Nanosheet for Ultrafast Photonics

Yan Lu [1,†], Zheng Zhou [2,†], Xuefen Kan [1], Zixin Yang [3], Haiqin Deng [3], Bin Liu [4], Tongtong Wang [4], Fangqi Liu [4], Xueyu Liu [1], Sicong Zhu [4], Qiang Yu [2,3,*] and Jian Wu [3,*]

1 School of Transportation Engineering, Jiangsu Shipping College, Nantong 226010, China
2 CAS Key Laboratory of Nanophotonic Materials and Devices & Key Laboratory of Nanodevices and Applications, i-Lab, Suzhou Institute of Nano-Tech and Nano-Bionics (SINANO), Chinese Academy of Sciences, Suzhou 215123, China
3 College of Advanced Interdisciplinary Studies, National University of Defense Technology, Changsha 410073, China
4 College of Science and Key Laboratory for Ferrous Metallurgy, Resources Utilization of Ministry of Education, Wuhan University of Science and Technology, Wuhan 430081, China
* Correspondence: qyu2015@sinano.ac.cn (Q.Y.); wujian15203@163.com (J.W.)
† These authors contributed equally to this work.

Abstract: The magnetic nanomaterial $Mn_3Si_2Te_6$ is a promising option for spin-dependent electronic and magneto-optoelectronic devices. However, its application in nonlinear optics remains fanciful. Here, we demonstrate a pulsed Er-doped fiber laser (EDFL) based on a novel quasi-2D $Mn_3Si_2Te_6$ saturable absorber (SA) with low pump power at 1.5 μm. The high-quality $Mn_3Si_2Te_6$ crystals were synthesized by the self-flux method, and the ultrathin $Mn_3Si_2Te_6$ nanoflakes were prepared by a simple mechanical exfoliation procedure. To the best of our knowledge, this is the first time laser pulses have been generated using quasi-2D $Mn_3Si_2Te_6$. A stable pulsed laser at 1562 nm with a low threshold pump power of 60 mW was produced by integrating the $Mn_3Si_2Te_6$ SA into an EDFL cavity. The maximum power of the output pulse is 783 μW. The repetition rate can vary from 24.16 to 44.44 kHz, with corresponding pulse durations of 5.64 to 3.41 μs. Our results indicate that the quasi-2D $Mn_3Si_2Te_6$ is a promising material for application in ultrafast photonics.

Keywords: $Mn_3Si_2Te_6$; magnetism; ultrafast photonics

Citation: Lu, Y.; Zhou, Z.; Kan, X.; Yang, Z.; Deng, H.; Liu, B.; Wang, T.; Liu, F.; Liu, X.; Zhu, S.; et al. Quasi-2D $Mn_3Si_2Te_6$ Nanosheet for Ultrafast Photonics. *Nanomaterials* **2023**, *13*, 602. https://doi.org/10.3390/nano13030602

Academic Editors: Iole Venditti and Harith Ahmad

Received: 30 December 2022
Revised: 19 January 2023
Accepted: 28 January 2023
Published: 2 February 2023

1. Introduction

The pulsed lasers in the communication band (1.5 μm) have an "eye safety" feature and low transmission loss in optical fiber. Owing to the large energy pulses, low cost, and compact structure, the 1.5 μm all-fiber short pulsed lasers have wide and momentous applications in LiDAR [1], remote sensing [2], supercontinuum spectrum [3], space communication [4], and biomedical diagnostics [5]. The passive Q-switching technique is one of the most effective methods to generate pulsed lasers [6–9]. By applying the Q-switched mechanism, short pulses can be achieved with durations of microseconds (μs) or nanoseconds (ns) and a low repetition rate of kilohertz (kHz) [10,11]. In this technique, the saturable absorbers (SAs) are essential components of fiber laser systems for modulating intracavity loss and generating short pulses [12]. Traditionally, doped crystals, e.g., Co:MALO [13], Cr:YAG [14], etc., are applied to fabricate commercially available passive Q-switching systems. However, the expensive manufacturing process and doping techniques restrict the further development of these crystal-based Q-switchers [15]. In addition, noble metal nanoparticles have also been advocated as SAs for attempting to build pulsed fiber lasers assisted by their localized surface plasmon resonance (LSPR) effect [16,17]. But the aggregation and non-uniformity of nanoparticles could reduce the pulsed laser's performance.

Over the past decade, numerous studies have been conducted developing two-dimensional (2D) van der Waals (vdWs) materials SAs to meet pulsed laser generation requirements [18], such as graphene [19,20], transition metal dichalcogenides (TMDCs) [21,22], topological insulators

(TIs) [23], black phosphorus (BP) [24–26], and MXenes [27,28]. These have been proven to have excellent optical properties and produce better laser pulse parameters. Due to the zero band gap, graphene has extremely weak photon absorption [29]. In 2010, Luo et al. used graphene in Er-doped fiber lasers for the first time to realize dual-wavelength pulse output with two wavelengths of 1566.17 nm and 1566.35 nm, respectively [30]. Compared with TMDCs, TIs have a wider wavelength response range, a higher damage threshold, and a greater modulation depth. In 2014, Lee et al. used Bi_2Te_3-SA integrated into a holmium-thulium co-doped fiber (THDF) laser to obtain stable pulses [31]. Soon after, BP was proven to have saturable absorption characteristics for the first time. Chen et al. integrated BP into EDF lasers as an SA to obtain pulse output [25]. Analogously, Shi et al. obtained a black arsenic-phosphorus (b-AsP) crystal with an adjustable band gap and designed an atomic ratio by the mineral-assisted chemical gas phase transport method in 2019, transferred it to the fiber facet to prepare a sandwich structure SA, and integrated it into the EDF laser. The output has a pulse width of 7.01 μs [32]. However, the above materials have flaws that limit their future application, such as low modulation depth, environmental instability, or complex preparation methods. Hence, it is urgent to explore novel SAs for pulsed lasers in ultrafast photonics and related applications.

In addition to 2D materials, many new-type low-dimensional nanomaterials as SA potential candidates have also attracted tremendous attention from the research community. For instance, the mode-locking pulse laser based on perovskite $CsCu_2I_3$ microrods SA exhibits ultra-stable properties [33], and the PbS-SA-based EDF pulse laser can realize the switch between Q-switched state and mode-locking state [34]. Moreover, many artificial SAs have also been designed to generate mode-locked pulse lasers, which have outstanding pulse output performance. In the future, artificial SAs may become a real alternative to natural SAs [35]. Because of the nonlinear optical properties of magnetic nanomaterials and their long relaxation times, they have also been proposed to be used as SAs to generate pulsed fiber lasers [36,37]. In 2016, Bai et al. first put forward applying the ferroferric oxide (Fe_3O_4) nanoparticles-based SA in pulsed EDF lasers, achieving a laser output wavelength of 1.55 μm and a laser output of 0.8 mW at a pump power of 110 mW, with a maximal pulse energy of 23.8 nJ, a repetition frequency of 33.3 kHz, and a pulse duration of 3.2 μs [38]. In 2018, the Fe_2O_3 nanoparticles were synthesized by a co-precipitation method, and then the thin Fe_2O_3 polyvinyl alcohol films were prepared to realize pulsed operations in three kinds of fiber lasers due to the broadband polarization-insensitive saturable absorption [39]. Quasi-2D $Mn_3Si_2Te_6$ nanosheets also exhibit stronger magnetism. Although their ferrimagnetic properties have been extensively studied, their equally interesting optical properties have been very limited. $Mn_3Si_2Te_6$ is unique in its atomic structure, and the resistivity ρ_a of the *ab* plane decreases by up to seven orders of magnitude only when the magnetic field H is applied along the magnetic hard c axis or the saturated magnetic state is not present [40,41]. Besides, the nonlinear optical properties allow for its utilization as an SA in a fiber-pulsed laser.

In this study, the premium $Mn_3Si_2Te_6$ crystals were prepared by the self-flux method, and the ultrathin $Mn_3Si_2Te_6$ nanoflakes were adopted as SAs for pulse generation. It has been demonstrated that a stable pulsed fiber laser at 1562 nm can be produced at a low threshold pump power of 60 mW. The maximum power of the output pulse is 783 μW. The repetition rate can vary from 24.16 to 44.44 kHz, with corresponding pulse durations of 5.64 to 3.41 μs. Our results indicate that the quasi-2D $Mn_3Si_2Te_6$ is a promising material for application in ultrafast photonics.

2. Fabrication and Characterization of $Mn_3Si_2Te_6$

2.1. Crystal Growth

By using the standard high-temperature self-flux method, single crystals of $Mn_3Si_2Te_6$ were grown. A mixture of Mn (powder, 99.95%; Aladdin Chemicals, Shanghai, China), Si (lump, 99.999%; Aladdin Chemicals, Shanghai, China), and Te (lump, 99.999%; Aladdin Chemicals, Shanghai, China) in a molar ratio of 1:2:6 was placed in an alumina crucible, and another empty alumina crucible was kept on top of it with quartz wool separation.

All the procedures handling the reagents were done in a glove box filled with highly pure argon gas. To achieve a homogeneous solution, the ampoule was heated to 1273 K in a muffle furnace for 10 h and then dwelled for 24 h. In the following 150 h, the furnace was cooled to 973 K slowly and then remained at 973 K for 24 h so that the crystals could be annealed. The crystals were then separated from the fluxes by centrifuging the ampoule, which had been quickly removed from the furnace. After centrifuging, the black single crystals of $Mn_3Si_2Te_6$ can be picked out from the remnants in the crucible. In most cases, after cleaning with isopropanol to remove impurities that are not completely crystallized on the surface, high-quality, shiny $Mn_3Si_2Te_6$ was harvested.

2.2. Apparatus and Characterization

$Mn_3Si_2Te_6$ has a trigonal crystal structure (spatial group No. 163), as shown in Figure 1a [42]. $Mn_3Si_2Te_6$ consists of $MnTe_6$ octahedrons that share edges within the *ab* plane (Mn1 site) and, together with Si-Si dimers, form layers of $Mn_3Si_2Te_6$. Similar to $CrSiTe_3$, which is hexagonal and has a vdWs gap between layers, the layered framework is hexagonal. Nonetheless, $Mn_3Si_2Te_6$ is composed of layers connected by Mn atoms at the Mn2 site, and these layers fill one-third of the octahedral holes within the vdWs gap to form $Mn_3Si_2Te_6$ [43]. Importantly, Mn1 has twice the multiplicity of Mn2 in comparison. In the unit cell, the lattice constants are $a = b = 7.029$ Å, and $c = 14.255$ Å. The Raman spectra (LabRAM HR Evolution, HORIBA, Villeneuve d'Ascq, France) of $Mn_3Si_2Te_6$ thin films are shown in Figure 1b, and a 532 nm laser is used as the excitation source in this characterization process. The four characteristic Raman peaks are identified at ~81 cm^{-1}, ~100 cm^{-1}, ~123 cm^{-1}, and ~141 cm^{-1}, respectively. This is different from the Raman data reported in the reference [44], and it could be attributed to detecting under different pressures. The characteristic peaks of the Raman spectrum of materials will be affected by the environment in which the materials are located. In ref. [44], the Raman spectrum of $Mn_3Si_2Te_6$ is measured under high pressure, whereas in this work it is measured under normal temperature and pressure, so there are differences. Figure 1c displays the main XRD spectra (AXS D8 Advance, Bruker, Billerica, MA, USA) characteristic peaks of high-crystallinity $Mn_3Si_2Te_6$. It matches the rhombohedral structure in space group P-3c1 (PDF # 01-074-1322). The peaks are (004), (006), (008), $(00\overline{10})$, and $(00\overline{12})$ respectively in $Mn_3Si_2Te_6$. The $Mn_3Si_2Te_6$ crystal is verified by the (00L) Bragg peaks, and the lattice parameters are determined as $a = b = 7.03$ Å and $c = 14.26$ Å by the powder X-ray diffraction of crushed crystals, which is consistent with previous reports [45].

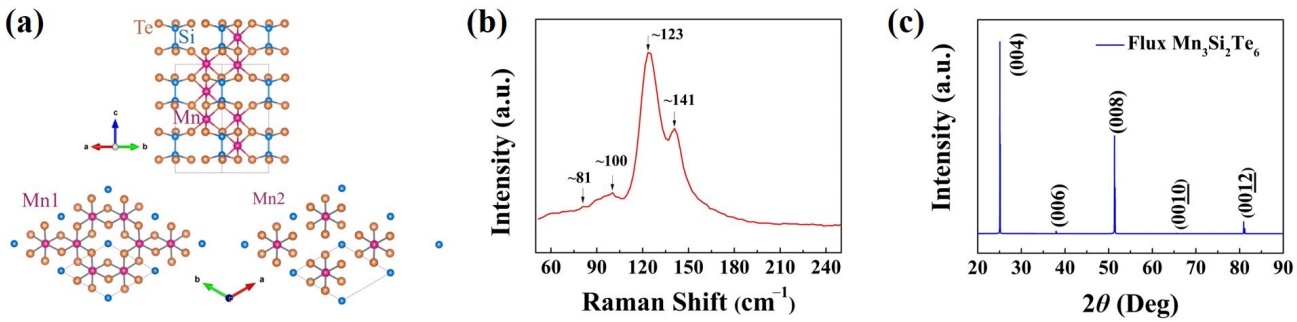

Figure 1. Crystal structure and characterizations: (**a**) crystal structure of $Mn_3Si_2Te_6$. The Mn atoms are located at the center of the $MnTe_6$ octahedra (colored regions), which stack along the *c* axis in honeycomb (Mn1) and triangular (Mn2) layers. (**b**) Raman spectra of $Mn_3Si_2Te_6$ single crystal at room temperature and 1 atm. (**c**) X-ray diffraction pattern of the $Mn_3Si_2Te_6$ crystal recorded on the (00L) plane at room temperature.

The ferrimagnetic properties of $Mn_3Si_2Te_6$ crystals are examined by a superconducting quantum interference device (MPMS3, 7T, Quantum Design, USA) in both in-plane and out-of-plane configurations. Figure 2a shows the magnetization *M* data of a $Mn_3Si_2Te_6$

single crystal when the applied magnetic field H lies in the ab plane ($H//ab$), and that M is significantly larger than that when $H//c$. We note that there are no remanent moments in either direction, which, in a way, indicates the high quality of the present single crystals. In accordance with this, the magnetization M rapidly saturates at $H//ab$, reaching ~1.35 μ_B/Mn at T = 2 K. Meanwhile, the zero-field cooling (ZFC) and field cooling (FC) tests at a 200 Oe magnetic field also show the typical ferromagnetic characteristics, as shown in Figure 2b. These data are broadly in line with the initial report about $Mn_3Si_2Te_6$ [46]. The observed Curie temperature of $Mn_3Si_2Te_6$ is $T_C \approx 78$ K. These results indicate that the material has distinct magnetic properties.

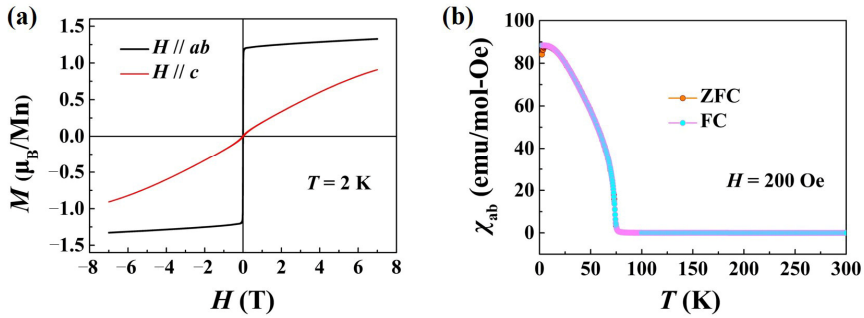

Figure 2. Ferrimagnetic properties of $Mn_3Si_2Te_6$: (**a**) M-H curves of $Mn_3Si_2Te_6$ bulk crystals at T = 2 K with magnetic fields along the in-plane ($H||ab$) and out-of-plane ($H||c$) directions, respectively. (**b**) ZFC-FC (H = 200 Oe, in-plane) curves of $Mn_3Si_2Te_6$ bulk crystals.

To study the nonlinear saturable optical absorption properties, the mechanically stripped $Mn_3Si_2Te_6$ nanosheet is transferred onto the end face of the fiber [47]. The specific dry transfer process is simple and convenient. First of all, the $Mn_3Si_2Te_6$ bulk was thinned by mechanical exfoliation with blue tape. When a suitable nanosheet has been identified, the underlying fiber end face is fixed on the moving stage. Finally, the tape is pressed against the fiber end face and peeled off very slowly. Figure 3a depicts the end face of the fiber following material transfer. Due to repeated mechanical stripping, in addition to the large nanosheet covering the fiber core, most of the surrounding nanosheets are small in size. The core position is completely covered by $Mn_3Si_2Te_6$ nanosheets and has been marked by red circles. The optical source of the two-arm detection system [48] is a pulsed laser with an operating wavelength of 1550 nm, a repetition frequency of 16.6 MHz, and a pulse duration of 448 fs.

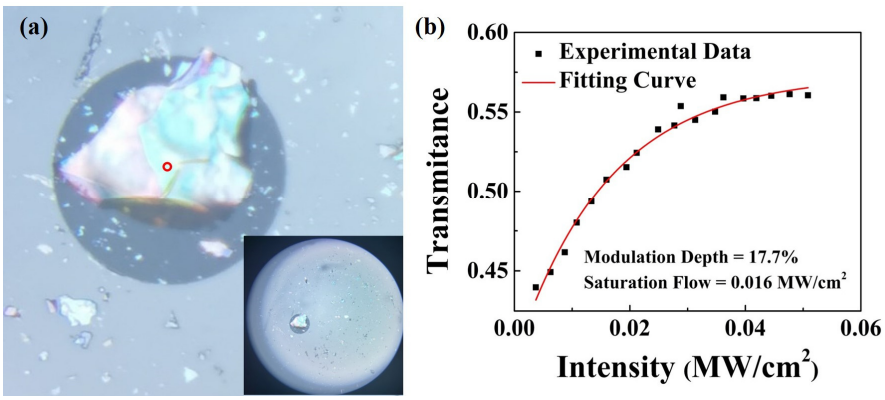

Figure 3. (**a**) $Mn_3Si_2Te_6$ saturable absorber on the edge of optical fiber. (**b**) nonlinear transmittance of the $Mn_3Si_2Te_6$ saturable absorber at different light intensities.

A simple saturation mode can describe the nonlinear optical absorption

$$T(I) = 1 - \Delta R \times \exp\left(-\frac{I}{I_s}\right) - T_{ns}$$

where $T(I)$ is the transmittance rate, ΔR is the modulation depth, and I, I_s, and T_{ns} are the input intensity, saturation intensity, and non-saturable absorbance, respectively. Figure 3b takes on the variation curve of nonlinear transmittance with laser energy intensity. By theoretical calculation, the modulation depth and saturation intensity of the $Mn_3Si_2Te_6$ SA are 17.7% and 16 kW/cm^2, respectively. It can be seen that the $Mn_3Si_2Te_6$ SA has a relatively small saturated power density, which also means that saturation can be formed at low power. On the contrary, more power will overflow at high power, which will have an unstable effect on the circulator.

3. Generation of the Short Fiber Pulsed Laser

Figure 4 shows the set-up diagram of the pulsed EDF laser that is based on $Mn_3Si_2Te_6$ SA, where the laser cavity has a ring-shaped design. Through 980/1550 wavelength division multiplexing (WDM), a 976 nm CW laser launched by a laser diode with the maximal power of 400 mW is coupled into the laser cavity as a pump. A 6-m-long EDF (LIEKKI: Er110-4-125) acted as the gain medium. The prepared $Mn_3Si_2Te_6$ SA is integrated into the laser cavity after the EDF. For unidirectional laser cavity operation, a polarization independent isolator (PI-ISO) is employed. The polarization state of circulating light is optimized using two polarization controllers (PCs). In the experimental operation, one PC always stays still and tunes only the other PC. Additionally, 20% of the pulsed laser power from the cavity is extracted by an optical coupler (OC). The cavity is approximately 11 m long, containing the EDF and tail fibers. A digital oscilloscope (Keysight DSOS104A, 1 GHz, USA), a spectrum analyzer (Yokogawa AQ6370D, Japan), and a power meter (Thorlabs DET08CFC/M, 5 GHz, USA) are utilized to determine the pulse trace, output spectrum, and average output power. The optical fiber is purchased from Yangtze Optical Fibre and Cable Joint Stock Limited Company (YOFC), and the optical fiber devices are purchased from CSRayzer Optical Technology. The illustration in Figure 4 shows the pulse trace at a pump power of 150 mW.

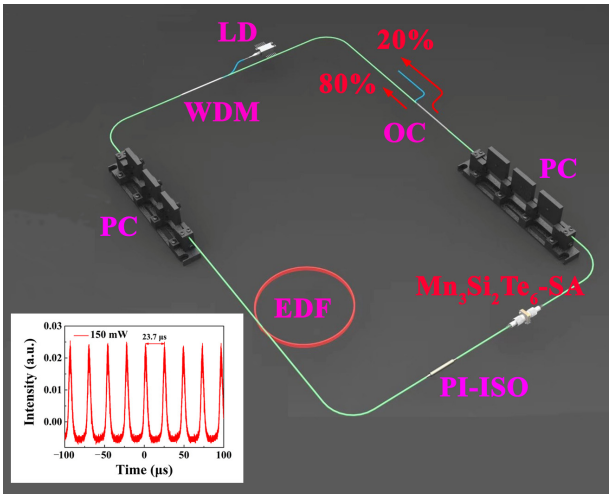

Figure 4. The schematic diagram of the pulsed fiber laser.

Figure 5a shows the pulse sequences versus different pump powers for the system that operates in a stable Q-switched state between 60 and 160 mW. The $Mn_3Si_2Te_6$ SA-based EDF pulse laser has high stability because the ferromagnetic material $Mn_3Si_2Te_6$ is highly stable in the air. Throughout the entire experiment period, even when $Mn_3Si_2Te_6$ SA is exposed to the air, the pulse sequence remains highly stable. Besides, when the laser is

turned off for several hours, we turn it back on, and it still produces a stable pulse laser sequence. Repeated operations can produce a stable pulse. Figure 5b depicts pulse-shaped spectra with soliton-like spectra at various pump powers. The spectrum shows different degrees of broadening. It is necessary to note that if the $Mn_3Si_2Te_6$ SA is removed by us in the experiment, the Q-switched pulse will not be generated. In addition, the central wavelengths of pulse lasers were always kept steady without drift when the two PCs were tuned simultaneously. It indicates that the PC does not play a leading role and that the number of PCs is not the main reason for the Q-switching phenomenon.

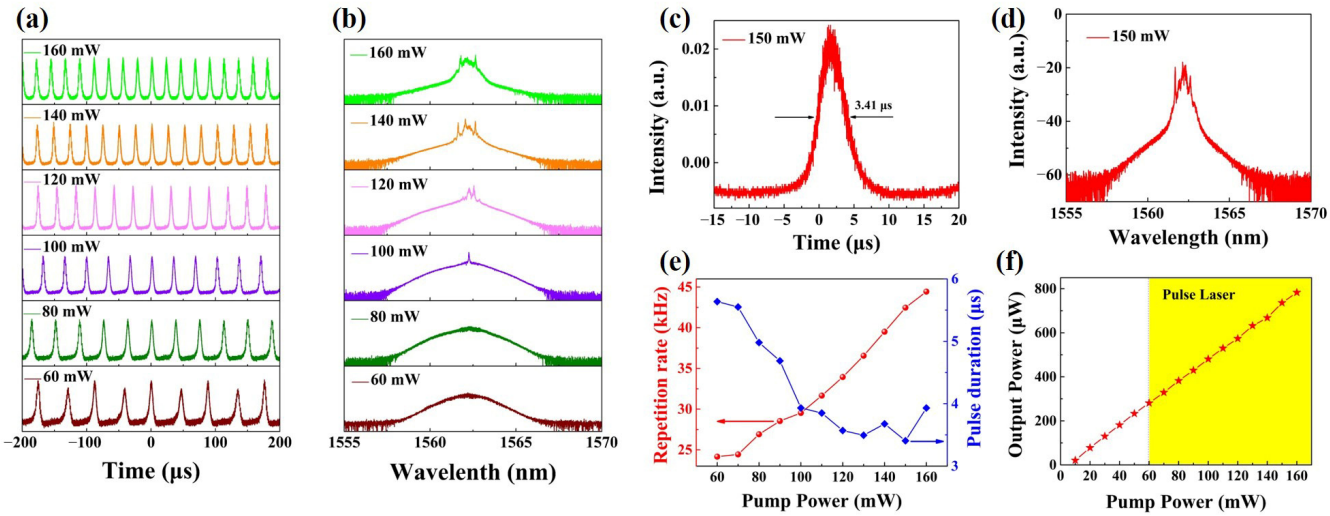

Figure 5. (**a**) pulse sequences. (**b**) the output spectra at given different pump powers. (**c**) the single pulse width at 150 mW pump power. (**d**) the output spectrum of the output pulse at 150 mW pump power. (**e**) repetition frequency and pulse duration as a function of pump power, and (**f**) the relationship between the average output powers and pump powers.

Figure 5c shows the characteristics of a stable single pulse at the pump power of 150 mW, and the corresponding output spectrum of the output pulse as shown in Figure 5d. By varying the pump power, as shown in Figure 5e, the repetition frequency and pulse width modulation ranges of 24.16 kHz to 44.44 kHz and 5.64 μs to 3.41 μs are observed, respectively. Besides, it should also be noted that the pulse duration can be further narrowed by decreasing the cavity length [12] and increasing the modulation depth of the $Mn_3Si_2Te_6$ SA.

The relationship between the average output powers and pump powers is depicted in Figure 5f. When the pump power is 160 mW, the average output power is up to 783 μW. Once this pump power is exceeded, the Q-switched operation state is destroyed and becomes unstable. This reason can be attributed to the oversaturation of the $Mn_3Si_2Te_6$ SA and the instability of the laser cavity [25]. Further modifications of cavity settings may further improve laser stability, thereby increasing pulse energy and peak power.

To further evaluate the potential of quasi-2D $Mn_3Si_2Te_6$ for ultrafast pulse generation, we compare the output performance of Q-switched fiber lasers based on several reported typical SAs (Table 1), such as graphene, black phosphorus (BP), black arsenic-phosphorus (b-AsP), Bi_2Se_3 topological insulator (TI), and Fe_3O_4 nanoparticles. The results show that quasi-2D $Mn_3Si_2Te_6$ has a narrower pulse width of 3.41 μs except for Fe_3O_4 nanoparticles. The narrow pulse width is the advantage of this $Mn_3Si_2Te_6$ SA-based EDFL. It should be noted that Fe_3O_4 nanoparticles are also a type of magnetic fluid material, and they exhibit the narrowest pulse width of 2.7 μs. Thus, it could be deduced that the magnetic properties of SA materials may help to reduce the pulse width. This point should be further researched in physics in the future. However, the output power of $Mn_3Si_2Te_6$ SA-based EDFL is far less than that of Fe_3O_4 nanoparticle SA-based EDFL. Although the output power of 783 μW based on $Mn_3Si_2Te_6$ SA is higher than the output power of ~145 μW based on Bi_2Se_3 TI SA, the lower output power will have an adverse effect on the practical application of this

pulsed laser. So, more efforts should be put into improving the output power of $Mn_3Si_2Te_6$ SA-based EDFL.

Table 1. Technical parameter comparison of several reported passive Q-switched EDFLs based on nanomaterial SA.

Materials	Gain Medium	Wavelength	Pulse Width	Repetition Rate	Pulse Energy	Pump Power	Output Power	Ref.
Graphene	Er-doped	1566.17 nm; 1566.35 nm	3.7 μs	65.9 kHz	16.7 nJ	6.5-82.8 mW	1.1 mW	[30]
BP	Er-doped	1562.87 nm	10.32 μs	15.78 kHz	94.3 nJ	50-195 mW	~1.5 mW	[25]
b-AsP	Er-doped	1559.9 nm; 1560.3 nm	5.26 μs	38.47 kHz	96.4 nJ	20-40 mW	3.68 mW	[32]
Bi_2Se_3 TI	Er-doped	1565.14 nm	13.4 μs	12.88 kHz	15 nJ	41.3-84.3 mW	~145 μW	[49]
Fe_3O_4 nanoparticles	Er-doped	1562.4 nm	2.7 μs	80 kHz	78.2 nJ	80-342 mW	6.23 mW	[37]
$Mn_3Si_2Te_6$	Er-doped	1562 nm	3.41 μs	44.44 kHz	-	60-160 mW	783 μW	This work

4. Conclusions

In summary, a quasi-2D $Mn_3Si_2Te_6$ nanosheet is successfully prepared, and its ferrimagnetic properties are studied. Meanwhile, a $Mn_3Si_2Te_6$-based SA is manufactured using a low-cost mechanical exfoliation method, and the nonlinear saturable optical absorption properties in the communication band are investigated. The modulation depth and saturation intensity of $Mn_3Si_2Te_6$ SA are calculated to be 17.7% and 16 kW/cm^2, respectively. Then, the prepared $Mn_3Si_2Te_6$ SA is integrated into a ring-shaped EDF laser cavity to successfully implement the pulsed operation for the first time. The laser pulses at 1562 nm were obtained with stability. The repetition frequency and pulse width modulation range are 24.16 kHz to 44.44 kHz and 5.64 μs to 3.41 μs, respectively, by varying the pump power from 60 mW to 160 mW. The maximal output power is 783 μW. This work certifies the potential of newly quasi-2D $Mn_3Si_2Te_6$ SA fabricated by low-cost mechanical exfoliation methods for ultrafast photonics applications.

Author Contributions: Conceptualization, Q.Y. and J.W.; methodology, Y.L., Z.Y. and X.K.; validation, X.L., H.D. and Z.Z.; investigation, F.L.; resources, Z.Z. and Q.Y.; writing—original draft preparation, Y.L.; writing—review and editing, Z.Z. and Q.Y.; visualization, B.L. and T.W.; supervision, Q.Y., S.Z. and J.W. All authors have read and agreed to the published version of the manuscript.

Funding: This research was funded by the China Postdoctoral Science Foundation, grant number 2021M702407; the Hubei Province Key Laboratory of Systems Science in Metallurgical Process, Wuhan University of Science and Technology, grant number Y202208; the Jiangsu Funding Program for Excellent Postdoctoral Talent; the Science and Technology Program Project of Nantong City, grant numbers MSZ20073 and JCZ21021; and the Science and Technology Project of Jiangsu Shipping College, grant number HYKY/2019B03.

Data Availability Statement: Not applicable.

Conflicts of Interest: The authors declare no conflict of interest.

References

1. Philippov, V.; Codemard, C.; Jeong, Y.; Alegria, C.; Sahu, J.K.; Nilsson, J.; Pearson, G.N. High-energy in-fiber pulse amplification for coherent lidar applications. *Opt. Lett.* **2004**, *29*, 2590–2592. [CrossRef] [PubMed]
2. Diaz, S.; Leandro, D.; Lopez-Amo, M. Stable multiwavelength erbium fiber ring laser with optical feedback for remote sensing. *J. Light. Technol.* **2015**, *33*, 2439–2444. [CrossRef]
3. Gopinath, J.T.; Shen, H.M.; Sotobayashi, H.; Ippen, E.P.; Hasegawa, T.; Nagashima, T.; Sugimoto, N. Highly nonlinear bismuth-oxide fiber for smooth supercontinuum generation at 1.5 μm. *Opt. Express* **2004**, *12*, 5697–5702. [CrossRef]
4. Doruk, E.; Slava, L.; Frank, K.; Kent, P.; Xung, D.; Jean-Luc, F.; Nigel, M.; Mark, S.; Shantanu, G.; Rich, U. Highly reliable and efficient 1.5um-fiber-MOPA-based, high-power laser transmitter for space communication. In Proceedings of the Laser Technology for Defense and Security X, SPIE, Baltimore, MD, USA, 5–9 June 2014; p. 90810G.
5. Liu, Y.; Gassino, R.; Braglia, A.; Vallan, A.; Perrone, G. Fibre probe for tumour laser thermotherapy with integrated temperature measuring capabilities. *Electron. Lett.* **2016**, *52*, 798–800. [CrossRef]

6. Liu, S.; Huang, H.; Lu, J.; Xu, N.; Qu, J.; Wen, Q. Liquid-Phase Exfoliation of Ta2NiS5 and Its Application in Near-Infrared Mode-Locked Fiber Lasers with Evanescent Field Interactions and Passively Q-Switched Bulk Laser. *Nanomaterials* **2022**, *12*, 695. [CrossRef]
7. Lin, H.; Bao, S.; Liu, X.; Song, S.; Wen, Z.; Sun, D. Dual-Wavelength Continuous-Wave and Passively Q-Switched Alexandrite Laser at 736.7 nm and 752.8 nm. *Photonics* **2022**, *9*, 769. [CrossRef]
8. Guo, X.; Wang, S.; Yan, P.; Wang, J.; Yu, L.; Liu, W.; Zheng, Z.; Guo, C.; Ruan, S. High Modulation Depth Enabled by Mo2Ti2C3Tx MXene for Q-Switched Pulse Generation in a Mid-Infrared Fiber Laser. *Nanomaterials* **2022**, *12*, 1343. [CrossRef]
9. Yang, Z.; Zaheer Ud Din, S.; Wang, P.; Li, C.; Lin, Z.; Leng, J.; Liu, J.; Xu, L.; Yang, Q.; Ren, X. Blue LD-pumped electro-optically Q-switched Pr:YLF visible laser with kilowatt-level peak power. *Opt. Laser Technol.* **2022**, *148*, 107711. [CrossRef]
10. Ahmad, H.; Reduan, S.A. Passively Q-switched S-band thulium fluoride fiberlaser with multi-walled carbon nanotube. *Chin. Opt. Lett.* **2018**, *16*, 010609. [CrossRef]
11. Meng, Y.; Liu, Y.; Li, T.; Feng, T.; Huang, J.; Ni, Z.; Qiao, W. Investigation of Nonlinear Optical Modulation Characteristics of MXene VCrC for Pulsed Lasers. *Molecules* **2022**, *27*, 759. [CrossRef]
12. Degnan, J.J. Optimization of passively Q-switched lasers. *IEEE J. Quantum Electron.* **1995**, *31*, 1890–1901. [CrossRef]
13. Yumashev, K.V.; Denisov, I.A.; Posnov, N.N.; Kuleshov, N.V.; Moncorge, R. Excited state absorption and passive Q-switch performance of Co2+ doped oxide crystals. *J. Alloys Compd.* **2002**, *341*, 366–370. [CrossRef]
14. Bai, Y.; Wu, N.; Zhang, J.; Li, J.; Li, S.; Xu, J.; Deng, P. Passively Q-switched Nd:YVO4 laser with a Cr4+:YAG crystal saturable absorber. *Appl. Opt.* **1997**, *36*, 2468–2472. [CrossRef] [PubMed]
15. Tang, C.Y.; Cheng, P.K.; Tao, L.; Long, H.; Zeng, L.H.; Wen, Q.; Tsang, Y.H. Passively Q-Switched Nd:YVO4 Laser Using WS2 Saturable Absorber Fabricated by Radio Frequency Magnetron Sputtering Deposition. *J. Light. Technol.* **2017**, *35*, 4120–4124. [CrossRef]
16. Kang, Z.; Liu, M.; Li, Z.; Li, S.; Jia, Z.; Liu, C.; Qin, W.; Qin, G. Passively Q-switched erbium doped fiber laser using a gold nanostars based saturable absorber. *Photonics Res.* **2018**, *6*, 549–553. [CrossRef]
17. Wang, X.-D.; Luo, Z.-C.; Liu, H.; Zhao, N.; Liu, M.; Zhu, Y.-F.; Xue, J.-P.; Luo, A.-P.; Xu, W.-C. Gold nanorod as saturable absorber for Q-switched Yb-doped fiber laser. *Opt. Commun.* **2015**, *346*, 21–25. [CrossRef]
18. Zhou, W.; Pang, X.; Zhang, H.; Yu, Q.; Liu, F.; Wang, W.; Zhao, Y.; Lu, Y.; Yang, Z. Frontier and Hot Topics of Pulsed Fiber Lasers via CiteSpace Scientometric Analysis: Passively Mode-Locked Fiber Lasers with Real Saturable Absorbers Based on Two-Dimensional Materials. *Materials* **2022**, *15*, 6761. [CrossRef]
19. Bao, Q.; Zhang, H.; Wang, Y.; Ni, Z.; Yan, Y.; Shen, Z.X.; Loh, K.P.; Tang, D.Y. Atomic-Layer Graphene as a Saturable Absorber for Ultrafast Pulsed Lasers. *Adv. Funct. Mater.* **2009**, *19*, 3077–3083. [CrossRef]
20. Wang, J.; Wang, Y.; Wang, T.; Li, G.; Lou, R.; Cheng, G.; Bai, J. Nonlinear Optical Response of Graphene Oxide Langmuir-Blodgett Film as Saturable Absorbers. *Nanomaterials* **2019**, *9*, 640. [CrossRef]
21. Zhang, H.; Lu, S.B.; Zheng, J.; Du, J.; Wen, S.C.; Tang, D.Y.; Loh, K.P. Molybdenum disulfide (MoS2) as a broadband saturable absorber for ultra-fast photonics. *Opt. Express* **2014**, *22*, 7249–7260. [CrossRef]
22. Wang, K.; Wang, J.; Fan, J.; Lotya, M.; O'Neill, A.; Fox, D.; Feng, Y.; Zhang, X.; Jiang, B.; Zhao, Q.; et al. Ultrafast Saturable Absorption of Two-Dimensional MoS2 Nanosheets. *ACS Nano* **2013**, *7*, 9260–9267. [CrossRef]
23. Zhao, C.; Zhang, H.; Qi, X.; Chen, Y.; Wang, Z.; Wen, S.; Tang, D. Ultra-short pulse generation by a topological insulator based saturable absorber. *Appl. Phys. Lett.* **2012**, *101*, 211106. [CrossRef]
24. Wang, T.; Zhang, W.; Wang, J.; Wu, J.; Hou, T.; Ma, P.; Su, R.; Ma, Y.; Peng, J.; Zhan, L.; et al. Bright/dark switchable mode-locked fiber laser based on black phosphorus. *Opt. Laser Technol.* **2020**, *123*, 105948. [CrossRef]
25. Chen, Y.; Jiang, G.; Chen, S.; Guo, Z.; Yu, X.; Zhao, C.; Zhang, H.; Bao, Q.; Wen, S.; Tang, D.; et al. Mechanically exfoliated black phosphorus as a new saturable absorber for both Q-switching and Mode-locking laser operation. *Opt. Express* **2015**, *23*, 12823–12833. [CrossRef] [PubMed]
26. Wang, T.; Jin, X.; Yang, J.; Wu, J.; Yu, Q.; Pan, Z.; Shi, X.; Xu, Y.; Wu, H.; Wang, J.; et al. Oxidation-Resistant Black Phosphorus Enable Highly Ambient-Stable Ultrafast Pulse Generation at a 2 mum Tm/Ho-Doped Fiber Laser. *ACS Appl. Mater. Interfaces* **2019**, *11*, 36854–36862. [CrossRef]
27. Jhon, Y.I.; Koo, J.; Anasori, B.; Seo, M.; Lee, J.H.; Gogotsi, Y.; Jhon, Y.M. Metallic MXene Saturable Absorber for Femtosecond Mode-Locked Lasers. *Adv. Mater.* **2017**, *29*, 1702496. [CrossRef]
28. Yang, Z.; Yang, Q.; Tian, Y.; Ren, X.; Li, C.; Zu, Y.; Zaheer Ud Din, S.; Gao, L.; Wu, J.; Chen, H.; et al. Few-layer Ti3CN MXene for ultrafast photonics applications in visible band. *J. Mater.* **2022**, *9*, 44–45. [CrossRef]
29. Zhang, Z.; Lin, P.; Liao, Q.; Kang, Z.; Si, H.; Zhang, Y. Graphene-Based Mixed-Dimensional van der Waals Heterostructures for Advanced Optoelectronics. *Adv. Mater.* **2019**, *31*, e1806411. [CrossRef]
30. Luo, Z.; Zhou, M.; Weng, J.; Huang, G.; Xu, H.; Ye, C.; Cai, Z. Graphene-based passively Q-switched dual-wavelength erbium-doped fiber laser. *Opt. Lett.* **2010**, *35*, 3709–3711. [CrossRef]
31. Jung, M.; Lee, J.; Koo, J.; Park, J.; Song, Y.-W.; Lee, K.; Lee, S.; Lee, J.H. A femtosecond pulse fiber laser at 1935 nm using a bulk-structured Bi_2Te_3 topological insulator. *Opt. Express* **2014**, *22*, 7865–7874. [CrossRef]
32. Shi, X.; Wang, T.; Wang, J.; Xu, Y.; Yang, Z.; Yu, Q.; Wu, J.; Zhang, K.; Zhou, P. Synthesis of black arsenic-phosphorus and its application for Er-doped fiber ultrashort laser generation. *Opt. Mater. Express* **2019**, *9*, 2348–2357. [CrossRef]

33. Deng, H.; Xu, X.; Liu, F.; Yu, Q.; Shu, B.; Yang, Z.; Zhu, S.; Zhang, Q.; Wu, J.; Zhou, P. Mode-locking Pulse Generation Based on Lead-free Halide Perovskite $CsCu_2I_3$ Micro-rods with High Stability. *J. Mater. Chem. C*, 2023; *Advance Article*. [CrossRef]
34. Guo, K.; Fan, C.; Yu, Q.; Wang, J.; Deng, H.; Wang, T.; Liu, F.; Ding, X.; Pan, Z.; Zhu, S.; et al. Time-domain flexible pulse fiber laser generation and high-power evolution based on inter-band excitation of lead sulfide nanoflakes. *Opt. Commun.* **2023**, *529*, 129065. [CrossRef]
35. Kobtsev, S.M. Artificial saturable absorbers for ultrafast fibre lasers. *Opt. Fiber Technol.* **2022**, *68*, 102764. [CrossRef]
36. Cai, K.; Zhang, X.; Wang, X.; Tong, C.; Wang, L. Broadband Tunable Passively Q-Switched Erbium-Doped ZBLAN Fiber Laser Using Fe_3O_4-Nanoparticle Saturable Absorber. *Appl. Sci.* **2022**, *12*, 9168. [CrossRef]
37. Mohammed, D.Z.; Khaleel, W.A.; Al-Janabi, A.H. Tunable Q-switched erbium doped fiber laser based on metal transition oxide saturable absorber and refractive index characteristic of multimode interference effects. *Opt. Laser Technol.* **2017**, *97*, 106–110. [CrossRef]
38. Bai, X.; Mou, C.; Xu, L.; Wang, S.; Pu, S.; Zeng, X. Passively Q-switched erbium-doped fiber laser using Fe_3O_4-nanoparticle saturable absorber. *Appl. Phys. Express* **2016**, *9*, 042701. [CrossRef]
39. Mao, D.; Cui, X.; He, Z.; Lu, H.; Zhang, W.; Wang, L.; Zhuang, Q.; Hua, S.; Mei, T.; Zhao, J. Broadband polarization-insensitive saturable absorption of Fe2O3 nanoparticles. *Nanoscale* **2018**, *10*, 21219–21224. [CrossRef]
40. Zhang, Y.; Ni, Y.; Zhao, H.; Hakani, S.; Ye, F.; DeLong, L.; Kimchi, I.; Cao, G. Control of chiral orbital currents in a colossal magnetoresistance material. *Nature* **2022**, *611*, 467–472. [CrossRef] [PubMed]
41. Sala, G.; Lin, J.Y.Y.; Samarakoon, A.M.; Parker, D.S.; May, A.F.; Stone, M.B. Ferrimagnetic spin waves in honeycomb and triangular layers of $Mn_3Si_2Te_6$. *Phys. Rev. B* **2022**, *105*, 214405. [CrossRef]
42. May, A.F.; Liu, Y.; Calder, S.; Parker, D.S.; Pandey, T.; Cakmak, E.; Cao, H.; Yan, J.; McGuire, M.A. Magnetic order and interactions in ferrimagnetic $Mn_3Si_2Te_6$. *Phys. Rev. B* **2017**, *95*, 174440. [CrossRef]
43. Vincent, H.; Leroux, D.; Bijaoui, D.; Rimet, R.; Schlenker, C. Crystal structure of $Mn_3Si_2Te_6$. *J. Solid State Chem.* **1986**, *63*, 349–352. [CrossRef]
44. Wang, J.; Wang, S.; He, X.; Zhou, Y.; An, C.; Zhang, M.; Zhou, Y.; Han, Y.; Chen, X.; Zhou, J.; et al. Pressure engineering of colossal magnetoresistance in the ferrimagnetic nodal-line semiconductor $Mn_3Si_2Te_6$. *Phys. Rev. B* **2022**, *106*, 045106. [CrossRef]
45. Liu, Y.; Hu, Z.; Abeykoon, M.; Stavitski, E.; Attenkofer, K.; Bauer, E.D.; Petrovic, C. Polaronic transport and thermoelectricity in $Mn_3Si_2Te_6$ single crystals. *Phys. Rev. B* **2021**, *103*, 245122. [CrossRef]
46. Rimet, R.; Schlenker, C.; Vincent, H. A new semiconducting ferrimagnet: A silicon manganese telluride. *J. Magn. Magn. Mater.* **1981**, *25*, 7–10. [CrossRef]
47. Jiang, K.; Ji, J.; Gong, W.; Ding, L.; Li, J.; Li, P.; Li, B.; Geng, F. Mechanical cleavage of non-van der Waals structures towards two-dimensional crystals. *Nat. Synth.* **2023**, *2*, 58–66. [CrossRef]
48. Wang, T.; Yu, Q.; Guo, K.; Shi, X.; Kan, X.; Xu, Y.; Wu, J.; Zhang, K.; Zhou, P. Sb_2Te_3 topological insulator for 52 nm wideband tunable Yb-doped passively Q-switched fiber laser. *Front. Inf. Technol. Electron. Eng.* **2021**, *22*, 287–295. [CrossRef]
49. Chen, Y.; Zhao, C.; Huang, H.; Chen, S.; Tang, P.; Wang, Z.; Lu, S.; Zhang, H.; Wen, S.; Tang, D. Self-Assembled Topological Insulator: Bi_2Se_3 Membrane as a Passive Q-Switcher in an Erbium-Doped Fiber Laser. *J. Light. Technol.* **2013**, *31*, 2857–2863. [CrossRef]